chemosensors

Article

Selective Determination of 4,4′-Oxydianiline (4,4′-ODA) in Plastic Packaging Using Molecularly Imprinted Polymer Sensor Integrated with Pyrolyzed Copper/Carbon Composite

Xuejun Zhou [1,*], Pengcheng Ye [1], Zhiding Huang [2], Chun Yang [1], Jiefang Ren [1], Jin Wang [1] and Shali Tang [1]

[1] Zhejiang Institute of Product Quality and Safety Science, Hangzhou 310018, China; janeyeah1998@163.com (P.Y.); yangc@zjzay.com (C.Y.); renjf@zjzay.com (J.R.); wangj@zjzay.com (J.W.); tangshali_77@163.com (S.T.)
[2] China Fiber Quality Monitoring Center, Beijing 100007, China; huangzhiding@126.com
* Correspondence: zhouxj@zjzay.com; Tel.: +86-0571-85129817

Abstract: This study focuses on the synthesis, fabrication, and characterization of a molecularly imprinted polymer (MIP) sensor tailored for the selective determination of 4,4′-oxydianiline (4,4′-ODA) in plastic products. Notably, by integrating the sensor matrix with pyrolyzed copper/carbon material derived from Cu-BTC MOF, a remarkable enhancement in electrochemical performance is achieved. The Cu-BTC material is grown successfully on the surface of carbon nanotubes (CNTs) and subjected to calcination at 800 °C, yielding a CNT/Cu/C composite. This composite exhibits an increased surface area and enhanced electron transfer capability, resulting in an improved current response. To augment the selective detection capability of the modified electrodes for 4,4′-ODA, molecularly imprinted polymers (MIPs) were incorporated onto the composite surface. The modified electrode (CNT-2/Cu/C/MIP/GCE) was synthesized using acrylamide (AM) and methacrylic acid (MAA) as dual-functional monomers with 4,4′-ODA as a template molecule via precipitation polymerization. The differential pulse voltammetric (DPV) current response to 4,4′-ODA showed a favorable linear relationship within the concentration range of (0.15–10 μM,10–100 μM), with a detection limit of 0.05 μM. Moreover, the CNT-2/Cu/C/MIP/GCE sensor demonstrates exceptional sensitivity, specificity, consistency, and durability. Furthermore, this approach has proven effective in detecting 4,4′-ODA in spiked nylon spatula samples, with recovery rates ranging from 86.3% to 103.5%.

Keywords: electrochemical sensor; molecularly imprinted polymer; 4,4′-Oxydianiline; Cu-BTC MOF; carbon nanotubes

Citation: Zhou, X.; Ye, P.; Huang, Z.; Yang, C.; Ren, J.; Wang, J.; Tang, S. Selective Determination of 4,4′-Oxydianiline (4,4′-ODA) in Plastic Packaging Using Molecularly Imprinted Polymer Sensor Integrated with Pyrolyzed Copper/Carbon Composite. *Chemosensors* **2024**, *12*, 121. https://doi.org/10.3390/chemosensors12070121

Received: 29 May 2024
Revised: 20 June 2024
Accepted: 25 June 2024
Published: 1 July 2024

1. Introduction

Plastic packaging materials play a crucial role in today's industries, and strict adherence to safety standards is necessary. However, concerns have arisen regarding the safety of food due to the potential transfer of Primary Aromatic Amines (PAAs) from packaging into food items. Primary Aromatic Amines (PAAs) are a series of organic compounds, commonly including benzidine, 2-naphthylamine, 4,4′-diaminodiphenylmethane, 4,4′-Oxydianiline, 4,4-diaminodiphenyl sulfide, 2,4,5-trimethylaniline, and 21 other kinds of substances, commonly used as intermediates for the synthesis of some compounds, such as azo dyes and antioxidants. These toxic chemicals are commonly found in polyurethane (PU) adhesives, food dyes, kitchen utensils, and rubber, and pose significant health risks. In particular, 4,4′-Oxydianiline (Oxy), one of the typical PAAs specified in REACH [1], was extensively utilized in dyeing processes of leather manufacturing as well as an intermediate in the manufacturing of epoxy resins. Regulatory bodies such as the European Commission and the U.S. Environmental Protection Agency (EPA) have imposed stringent regulations [2,3] to restrict the presence of PAA residues in consumer goods due to the

health hazards associated with exposure to PAAs, including carcinogenicity and mutagenicity [4,5]. According to European Regulation 1416/2016, plastic materials and articles shall not release PAAs in detectable quantities into food or food simulants. The total migration for the PAAs not listed in REACH shall not exceed 0.01 mg/kg food or food simulant. However, the illegal use of azo dyes, which can transform into carcinogenic aromatic amines, persists due to their cost-effectiveness and antimicrobial properties. The molecule 4,4′-Oxydianiline is toxic to aquatic organisms. Its toxicity is listed by the EPA [6] as LC 50 for Ceriodaphnia dubia, Pimephales promelas (Fathead minnow), and Selenastrum capricornutum (algae). The concentrations are 223.6 µg/L for 48 h, 22 mg/L for 96 h, and 7.9 mg/L for 72 h. Therefore, there is an immediate requirement for precise, prompt, and efficient analytical methods to detect PAAs. Although several technological methods are available to identify derivatives of aromatic amines, such as gas chromatography [7], fluorescence spectroscopy [8], ultraviolet spectrophotometry [9], and liquid chromatography [10], they are often impeded by their high cost and complexity.

Molecular imprinting technology (MIT) is a promising option for specific detection in sensor technology due to its simplicity, strong selectivity, and durability. Molecularly imprinted polymers (MIPs) are designed with cavities complementary to template molecules [11–14] and offer a wide range of applications, including enrichment and separation [15–17], biosensors [18,19], biomimetic antibodies [20], and electrochemical detection [21]. In recent years, MIPs based on template imprinting have been employed for the recognition and extraction of aromatic amines [22–30]. For instance, Liu et al. synthesized a MIP using 4,4′-methylenedianiline as the template and applied it for electrochemical detection of 4,4′-methylenedianiline in food-contact materials [27]; Dang et al., developed an MIPs–PTSPE combined with HPLC method for selective recognition and determination of six aromatic amines in polyamide food contact materials [30]. Conventional molecularly imprinted polymers (MIPs) suffer from poor conductivity, which results in low sensitivity in electrochemical sensors. To address this issue, researchers have employed nanocomposites consisting of metal–organic frameworks (MOFs) and carbon nanotubes (CNTs) to enhance sensor conductivity. MOFs are known for their porous structure and high specific surface area, while CNTs boast superior electrical conductivity and biocompatibility. Through high-temperature carbonization, MOFs serve as ideal precursors for building advanced graphitized carbon-based electrode materials.

This study focuses on the development of a molecularly imprinted electrochemical sensor modified with a CNT/Cu/C coating for the analysis of 4,4′-oxydianiline (4,4′-ODA). The resulting sensor exhibits enhanced conductivity and current response, making it highly sensitive, selective, reproducible, and stable. By utilizing electrochemical techniques, such as cyclic voltammetry and differential pulse voltammetry, this sensor offers a practical solution for detecting 4,4′-ODA in plastic packaging materials. The simplicity of its design and its compatibility with practical applications in food safety underscores its potential significance.

In summary, this study aims to advance the understanding of MIPs in creating highly sensitive electrochemical sensors and suggests avenues for further research in this domain. The insights gained are expected to foster the development of more reliable strategies for detecting 4,4′-ODA and other harmful food additives, thereby contributing to food safety and quality control efforts.

2. Materials and Methods

2.1. Chemicals and Apparatus

Analytical grade chemicals, including copper nitrate trihydrate, trimesic acid, polyvinylpyrrolidone (PVP), carbon nanotubes (CNTs), and various solvents, such as methanol, ethanol, acetic acid, acetonitrile, and DMF, were procured from Sinopharm Chemical Reagent Co., Ltd. (Shanghai, China). Additionally, 4,4′-oxydianiline (4,4′-ODA), azobisisobutyronitrile (AIBN), ethylene glycol dimethacrylate (EGDMA), acrylamide (AM), and methacrylic acid (MAA) were obtained from Taitan Technology Co., Ltd. (Shanghai,

China). A phosphate-buffered saline (PBS) solution was prepared by mixing potassium dihydrogen phosphate, dipotassium hydrogen phosphate, and ultrapure water.

Fourier transform infrared (FT-IR) spectroscopy was performed using a Nicolet IS50 FT-IR spectrometer (Thermo Fisher Scientific, Madison, WI, USA) within the range of 4000–400 cm^{-1}. Powder X-ray diffraction (PXRD) measurements were conducted on an Ultima IV diffractometer with Cu-Kα radiation (λ = 1.5418 Å) in the range of 10–80°. The morphology and structure were analyzed using scanning electron microscopy (SEM) (JEOL JSM 6510) (JEOL, Akishima-shi, Tokyo, Japan) and transmission electron microscopy (TEM) (JEOL TEM 2100) (JEOL, Akishima-shi, Tokyo, Japan). X-ray photoelectron spectroscopy (XPS) analysis was performed using an ESCA Lab 250 spectrometer from Thermo in Shanghai, China, with a monochromatic Al Kα excitation source at 1486.6 eV. Cyclic voltammetry (CV), differential pulse voltammetry (DPV), and electrochemical impedance spectroscopy (EIS) were conducted using Zahner-Zennium Pro (Kronach, Gundelsdorf, Germany). The electrochemical cell employed in this study was comprised of a glassy carbon electrode (GCE), with a diameter of 2 mm and modified with various electrochemical materials, acting as the working electrode; a platinum electrode as the auxiliary electrode; and an Ag/AgCl electrode as the reference electrode.

2.2. Sample Preparation

The CNT-n/Cu-BTC composite was synthesized by dissolving 0.9 g of $Cu(NO_3)_2 \cdot 3H_2O$ and 0.4 g of polyvinylpyrrolidone (PVP) in 50 mL of methanol. Then, 0.43 g of 1,3,5-benzenetricarboxylic acid (BTC) was dissolved in 50 mL of methanol. The two solutions were mixed to form a homogeneous solution. Various amounts of CNTs (0.05, 0.1, 0.2, 0.3, 0.4 g) were dispersed into the mixed solution, which was vigorously stirred for 10 min. The suspension was aged for 24 h, then subjected to centrifugation and three washes in methanol and ethanol. Afterward, the resulting samples were dehydrated in a vacuum oven overnight at 60 °C. The products were designated as CNT-1/Cu-BTC to CNT-5/Cu-BTC based on the amount of CNT added. Furthermore, pure Cu-BTC was prepared using a similar method without the addition of CNTs. Subsequently, specific amounts of CNT-n/Cu-BTC were calcined at 800 °C for 12 h in a continuous N_2 flow, with a heating rate of 5 °C/min. This resulted in the production of the CNT-n/Cu/C product.

2.3. Preparation of MIP, CNT-n/Cu/C/MIP/GCE

A solution was prepared by dissolving 5 mM 4,4′-ODA, 15 mM acrylamide, and 15 mM methacrylic acid in a mixture of 20 mL dimethyl sulfoxide and 100 mL acetonitrile. The solution was sonicated for 30 min and then incubated for 24 h at 4 °C. Next, 0.125 g of azobisisobutyronitrile and 1.25 mL of ethylene glycol dimethacrylate were added to 50 mL of the mixture, followed by sonication for one hour. A suspension of MIP with 4,4′-ODA was produced by subjecting the solution to N_2 gas for 30 min and agitating at 65 °C for 24 h, after eliminating oxygen. The suspension was washed with ethanol and water after centrifugation and then dried under vacuum at 65 °C. The dried solid was eluted with a methanol–acetic acid solution (8:2 v/v) under stirring, then dried under vacuum at 60 °C to yield a MIP powder without template molecules. Similarly, a non-imprinted polymer (NIP) was created without including 4,4′-ODA.

Before modification, the uncoated GCE was polished with 50 nm Al_2O_3 powder on chamois leather. Subsequently, it was treated with EtOH and nitric acid solutions (v/v, 1:1) through sonication. The electrode was washed and dried at room temperature. A combination of 480 µL water, 480 µL ethanol, and 40 µL naphthol (total volume of 1 mL) was used to disperse the CNT-n/Cu/C (0.005 g), while 1 mL water was used to disperse the MIPs (0.005 g). After sonication for 30 min, a 6 µL droplet of the CNT-n/Cu/C suspension was dip-coated onto the GCE surface and left to dry at ambient temperature. Next, 6 µL of the MIP suspension was applied and allowed to dry at room temperature, resulting in the formation of CNT-n/Cu/C/MIP/GCE.

2.4. Electrochemical Measurements

Cyclic voltammetry was conducted within the voltage range of from −0.2 V to 0.6 V compared to Ag/AgCl, using a scan rate of 50 mV/s in a 0.1 M KCl solution with 5 mM $K_3Fe(CN)_6/K_4Fe(CN)_6$. Electrochemical impedance spectroscopy (EIS) tests were performed in a 0.1 M KCl solution with 5 mM $K_3Fe(CN)_6/K_4Fe(CN)_6$, covering a frequency range of from 0.1 Hz to 100.0 kHz. The DC and AC voltages were 0 V and 10 mV. Differential pulse voltammetry (DPV) was conducted in a 0.1 M phosphate-buffered saline (PBS) solution with a pH of 7, using varying quantities of 4,4′-ODA. The DPV parameters were as follows: start potential: −0.9 V; end potential 0.1 V; potential step 5 mV; pulse width 50 ms; pulse period 200 ms.

2.4.1. Analytical Application Tests of the Sensor

The CNT-2/Cu/C/MIP/GCE electrode was modified and utilized to quantitatively detect 4,4′-ODA under optimized experimental conditions. A quantitative analysis was conducted using differential pulse voltammetry (DPV) in a phosphate-buffered saline (PBS) solution with a pH of 7. The concentration range of 4,4′-ODA was from 0.15 µM to 10 µM and from 10 µM to 100 µM.

2.4.2. Evaluation of the Sensor's Selectivity

The specificity of the CNT-2/Cu/C/MIP/GCE electrochemical sensor towards 4,4′-ODA was evaluated by differential pulse voltammetry (DPV) current responses of 10 µM 4,4′-ODA and 100 µM (methionine, 4,4′-methylenedianiline, biphenyl, urea, benzidine) in a phosphate-buffered saline (PBS) solution.

2.4.3. Reproducibility and Stability of the Sensor

The reproducibility of the CNT-2/Cu/C/MIP/GCE electrochemical sensor was evaluated by DPV response towards 10 µM 4,4′-ODA with five different electrodes. The stability of the sensor was subjected to continuous testing every seven days for a period of 28 days.

2.5. Real Sample Test

The performance of the modified electrode was assessed in real-world conditions according to the methodology described in the Chinese National Standard GB 31604.52-2021 [31]. Nylon spatula samples, each with a surface area of 1.8 square decimeters, were submerged in a 300-milliliter solution containing 10% volume/volume ethanol in water. The samples were conventionally sterilized by heating them at 100 °C for 60 min using a heating and drying oven. The migration test was repeated three times. The soaking solution obtained from the third migration was used for further experimentation. After sterilization, 4,4′-ODA was added to a 20 mL soaking solution with PBS in a 1:1 ratio. The concentration of 4,4′-ODA was measured using amperometry to determine the final recovery rate of the substance.

3. Results

3.1. Material Characterizations

The functional groups present in the synthesized material were characterized by performing chemical analysis on the created sensor, utilizing ATR-FTIR spectra in the range of 4000–400 cm^{-1}. Figure 1 illustrates the FTIR spectra displaying specific peaks of 4,4′-ODA at 3440, 1638, 1500, and 800 cm^{-1}, representing -NH_2 stretching, aromatic C-N heterocycle stretching, C-O-C stretching, and aromatic C-C stretching, respectively [32]. The FTIR spectra of both molecularly imprinted polymers (MIPs) and non-imprinted polymers (NIPs) exhibited a similar pattern due to their analogous structures. Both spectra showed bands at 2955, 1720, 1455, 1389, 1252, and 1150 cm^{-1}, respectively. The absorption band at 2955 cm^{-1} can be attributed to the presence of C-H stretching in the polymer network, while the band at 1720 cm^{-1} corresponds to asymmetric stretching vibration modes of the carbonyl group (C=O) [28]. The band at 1455 cm^{-1} indicates C=C stretching of

aromatic hydrocarbons, while the bands at 1389, 1252, and 1150 cm^{-1} signify aromatic C-N, C-C, and C-O stretching vibration, respectively [30]. These results confirm the successful incorporation of the functional monomer into the polymeric matrix.

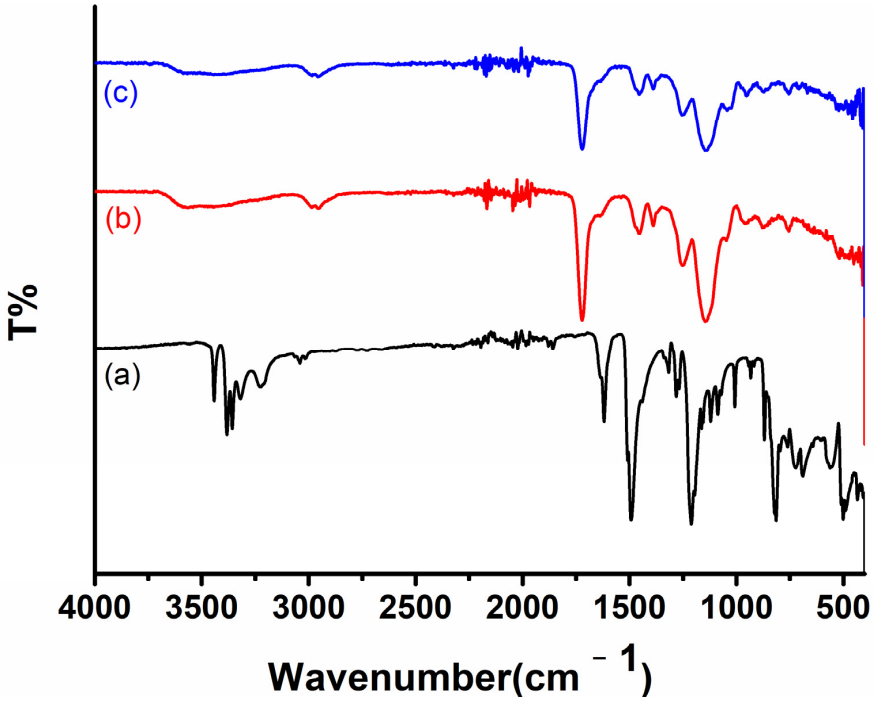

Figure 1. The ATR-FTIR spectra of (a) 4,4′−ODA, (b) MIP, and (c) NIP surfaces.

XRD powder patterns were obtained to analyze the structures of the prepared samples (see Figure 2). The XRD pattern of Cu-BTC is consistent with previously reported data [33]. The observed diffraction peaks at 26.6°, 43.0°, 44.7°, 50.8°, and 54.8° correspond to the (004), (101), (102), (104), and (008) planes of CNT [34,35], respectively, which are consistent with standard data (JCPDS 26-1080). Representative CNT-2/Cu-BTC was selected for further calcination at 800 °C in a nitrogen atmosphere, followed by XRD analysis. Upon calcination, the peaks corresponding to the (222), (400), (551), and (440) planes of Cu-BTC disappeared at 11.6°, 13.4°, 17.6°, and 20.4°, respectively. Instead, three distinct diffraction peaks appeared at angles of 26.6°, 43.3°, 50.4°, and 74.1°, representing the (004) crystal planes of hexagonal carbon (JCPDS 26-1080) and the (111), (200), and (220) crystal planes of face-centered cubic (fcc) Cu (JCPDS 04-0836) [36].

SEM and TEM microscopy were used to analyze the morphology of the synthesized hybrid nanocomposites. The SEM images of the CNT-2/Cu-BTC sample reveal the presence of octahedral Cu-BTC nanoparticles (NPs), with particle sizes of approximately 400 nm, distributed and closely attached to the surface of CNTs (Figure 3a). This observation indicates the successful growth of Cu-BTC on the surface of CNTs. Subsequently, the CNT-2/Cu-BTC sample was calcined at 800 °C to produce CNT-2/Cu/C material. As shown in Figure 3b, the CNT-2/Cu/C material maintains the octahedral morphology of Cu-BTC, but with smaller particle sizes, and the tubular morphology of CNT. The overall framework composition remains the same after calcination, as evidenced by the high-angle annular dark-field transmission electron microscopy (HAADF-TEM) images of CNT/Cu/C (Figure 3d). Additionally, the hybrid sample shows an even distribution of Cu, N, and C elements at the nanometer scale, as revealed by elemental mapping (Figure 3e–g). The Cu and C elements are a result of the calcination and decomposition of CNT-2/Cu-BTC composites, while the N element originates from the calcination and decomposition of residual polyvinylpyrrolidone (PVP), which may have participated in complexation with the Cu-BTC composite. The HRTEM image in Figure 4 shows octahedral Cu NPs surrounded by amorphous carbon and tubular CNT nanotubes. The spacing between

lattice fringes, measuring 0.21 nm, corresponds to the (111) orientation of Cu, which is consistent with the findings from XRD analysis.

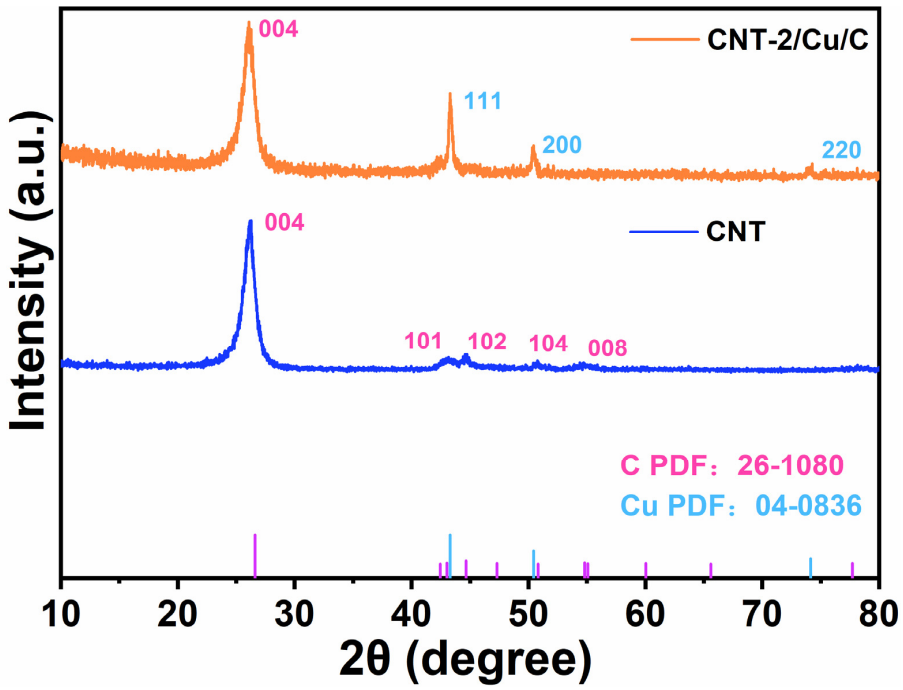

Figure 2. XRD patterns of the CNT/Cu/C samples.

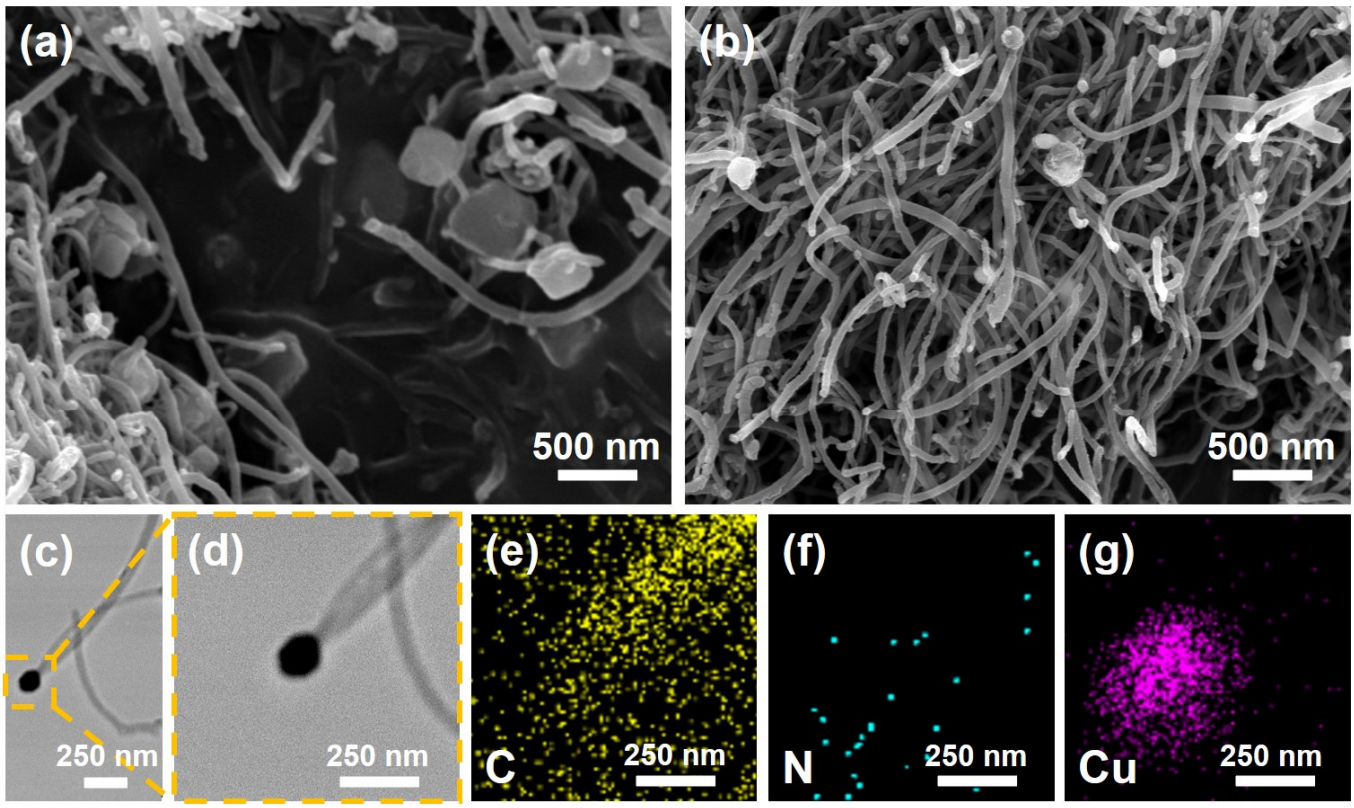

Figure 3. SEM and TEM spectra were obtained for each modified material, including CNT-2/Cu-BTC (**a**), CNT-2/Cu/C (**b**), and HAADT-STEM images of CNT-2/Cu/C (**c**,**d**), as well as elemental mapping images of the CNT-2/Cu/C composite (**e**–**g**).

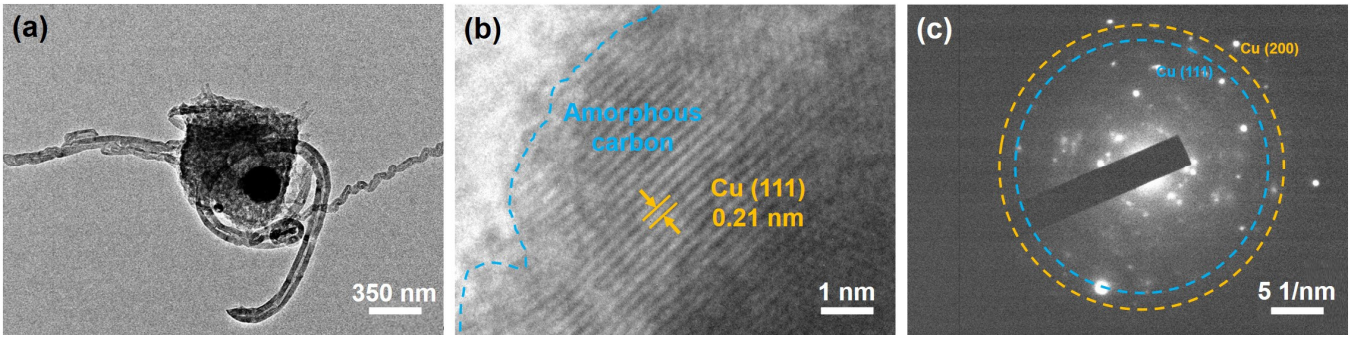

Figure 4. TEM images (**a**), HRTEM image (**b**), and theSAED pattern (**c**) of CNT-2/Cu/C composite.

The MIPs obtained through the precipitation polymerization method exhibit a spherical morphology, as shown in Figure 5a. The modified electrodes are more sensitive due to the selective recognition of 4,4′-ODA through hydrogen bonding. The SEM image in Figure 5b reveals a rough surface on the electrode, that has been modified using CNT/Cu/C/MIP/GCE, containing numerous voids. These voids facilitate electron transfer and enhance the electrochemical reaction to 4,4′-ODA.

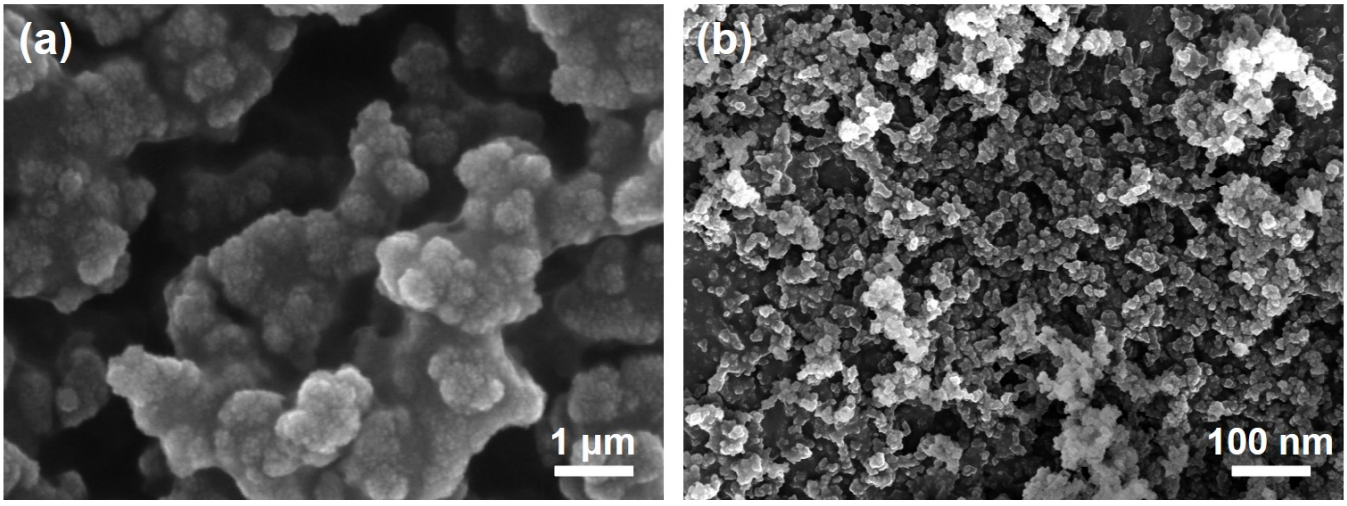

Figure 5. SEM images of MIP (**a**) and CNT-2/Cu/C/MIP/GCE (**b**).

XPS measurements were utilized to investigate the chemical states and surface composition of the elements. The survey analysis of CNT-2/Cu/C reveals the presence of Cu, C, N, and O elements, consistent with the elemental mapping findings (Figure 6a). The peaks detected at 284.8 eV, 285.4 eV, and 286.6 eV correspond to the C-C bond, C-N bond, and C-O bond, respectively, in the C 1s spectrum (Figure 6b) [37]. The generation of C-O primarily stems from the oxidation of carbon materials, while MOF materials exhibit high porosity, which promotes increased exposure to air and facilitates extensive interaction with ions in solution during reactions. The N 1s spectrum (Figure 6c) shows peaks at 398.7 eV, 401.1 eV, and 403.3 eV, corresponding to pyridinic N, graphitic N, and oxidized N, respectively [38]. This indicates the successful introduction of nitrogen into the material (consistent with the mapping results mentioned above), and the incorporation of nitrogen effectively enhances the material's electrical conductivity [39]. Figure 6d displays the Cu 2p spectrum, with peaks at 932.2 eV and 934.7 eV representing Cu 2p3/2, and peaks at 954.8 eV and 952.5 eV representing Cu 2p1/2 [40]. These results confirm the successful decoration of Cu-BTC MOFs using the CNT-based platform.

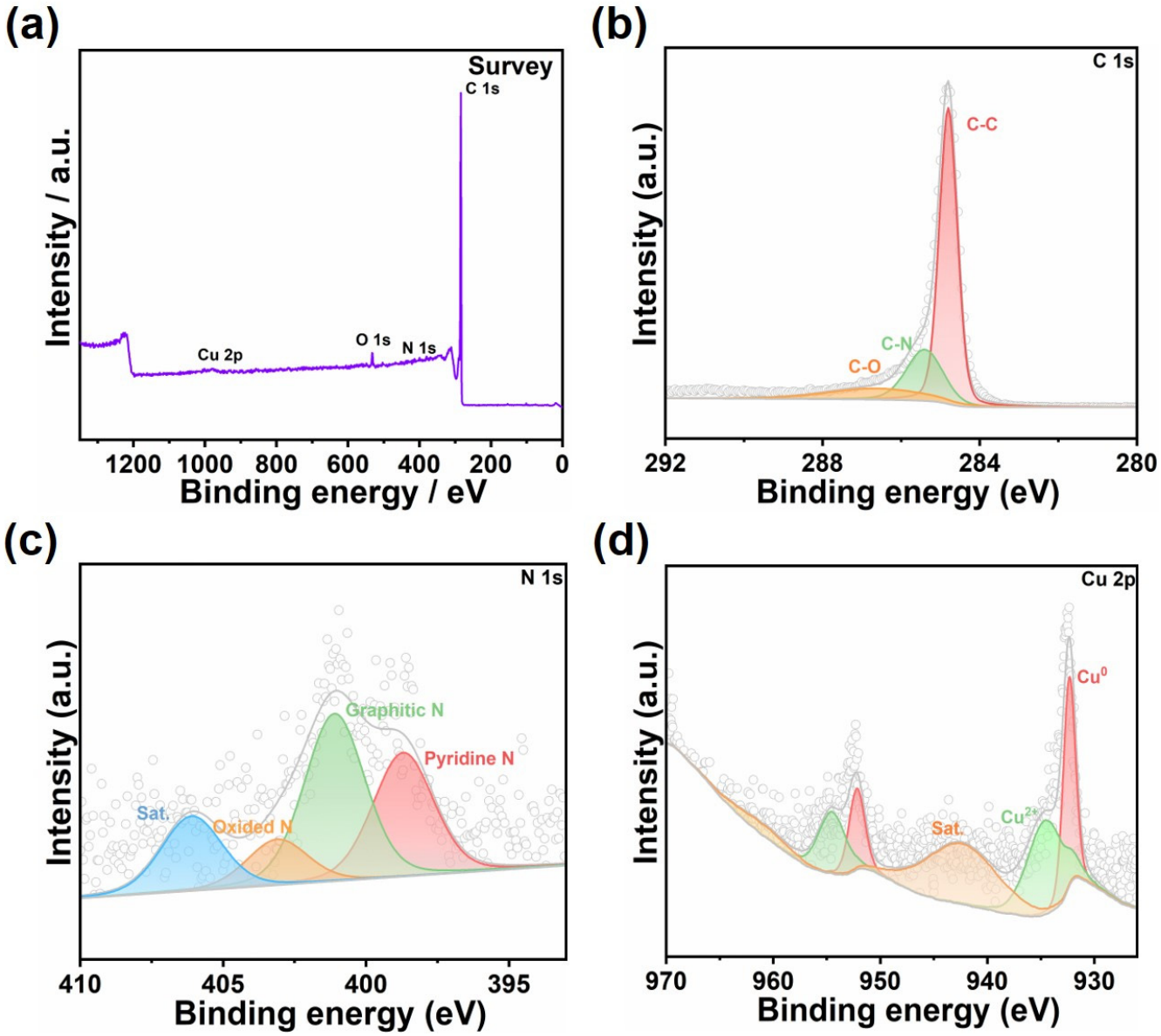

Figure 6. The XPS survey spectrum (**a**) and XPS analysis of CNT-2/Cu/C revealed peaks for the C 1s (**b**), N 1s (**c**), and Cu 2p (**d**).

To gain a better understanding of the electron-transfer conductivity of the modified electrode, Raman scattering spectra were recorded and the results can be seen in Figure 7. It has been demonstrated that defects inherent to carbon surfaces are crucial active sites for conducting electricity. The significant flaw in graphitic carbon can lower electrical conductivity, hindering the movement of carriers and transfer of charge. Figure 7 shows the Raman spectrum of the calcination process resulting in the CNT-n/Cu/C materials. The spectrum displays two characteristic bands: the D band at 1345 cm^{-1} and the G band at 1589 cm^{-1}. The D band signifies inherent defects and irregularities in carbon materials, while the G band indicates the graphitization process. The intensity ratio of the D and G bands can be used to determine the degree of defects/orders. The CNT-2/Cu/C with the lowest I_D/I_G ratio of 0.49 exhibited the best electrochemical property due to the presence of more graphitic carbon. It is widely accepted that a higher degree of graphitization results in greater electrical conductivity of carbon materials, making it easier to expose the active sites.

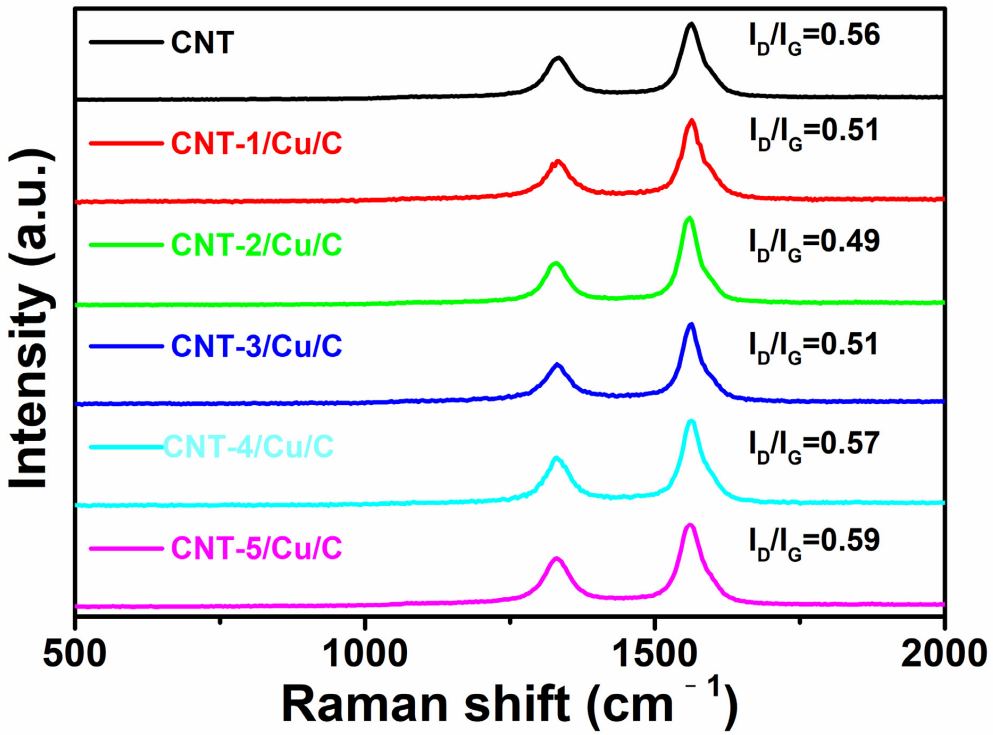

Figure 7. The Raman spectra of CNT-n/Cu/C materials with different I_D/I_G.

3.2. Electrochemical Behavior

The Cyclic voltammetry (CV) testing was performed on various electrodes, including bare GCE, CNT/GCE, Cu/C/GCE, CNT-n/Cu/C/GCE, CNT-2/Cu/C/NIP/GCE, CNT-2/Cu/C/MIP/GCE before elution, and CNT-2/Cu/C/MIP/GCE (after elution), to examine their electrochemical characteristics. They were measured in a 0.1 M KCl solution containing 5 mM $K_3Fe(CN)_6/K_4Fe(CN)_6$. As illustrated in Figure 8a, the Cu/C/GCE electrode exhibited a peak current of 68 μA. With the increase in CNT content, the peak shifted negatively, and the peak current exhibited a notable increase, which subsequently declined. This suggests that the appropriate Cu/C modification can effectively enhance the increase in active sites. As shown in Figure 8b, a comparison of several major curves is presented. The bare electrode exhibited a distinct pair of redox peaks of potassium ferricyanide with a peak current of 18 μA. By comparing the test results in the figure, it can be observed that the peak intensity of sample CNT-2/Cu/C/GCE (176 μA) is significantly higher than CNT/GCE, and approximately 10 times higher than that of the bare GCE, indicating that modifying the CNT surface with Cu/C can effectively enhance the electrode's performance. Furthermore, compared to the CNT-2/Cu/C/NIP/GCE and CNT/MIP/GCE, the electrode with introduced MIP after elution (CNT-2/Cu/C/MIP/GCE 220 μA) shows a greater peak intensity, demonstrating its effectiveness in increasing electron conductivity during the process. The CNT-2/Cu/MIP/GCE before elution exhibited significantly lower values because MIP possesses more imprinting cavities on its surface, accelerating the electron transfer of the $[Fe(CN)_6]^{3-/4-}$ probe.

Electrochemical impedance spectroscopy (EIS) was performed on each modified electrode to analyze its electron transfer properties. The internal resistances associated with the electron transfer mechanism were evaluated using the arc radius of the EIS Nyquist plot. A smaller radius of curvature generally indicates a greater ability for electron transfer. Figure 9a shows a significant decrease in the resistance of CNT-2/Cu/C/GCE compared to the other electrodes. This is due to the composite's excellent electrical conductivity. From Figure 9b, it can be seen that the introduction of MIP increases the electrode's resistance due to the poor conductivity of MIP; however, its resistance is still lower compared to other electrodes with MIP.

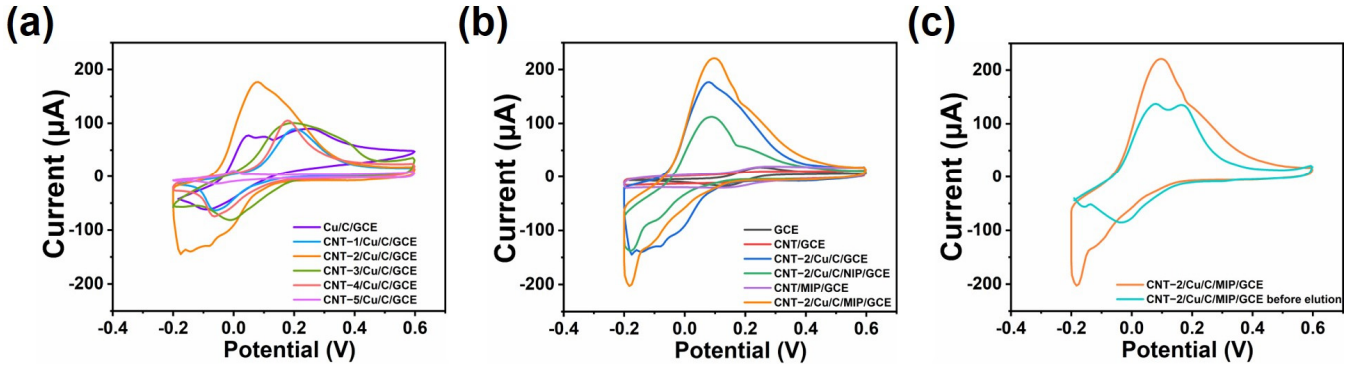

Figure 8. The CV plots for each electrode modification were obtained in a solution containing 5 mM $[Fe(CN)_6]^{3-/4-}$ and 0.1 M KCl. (**a**) The plots included a GCE modified with Cu/C, CNT-1/Cu/C, CNT-2/Cu/C, CNT-3/Cu/C, CNT-4/Cu/C, and CNT-5/Cu/C; (**b**) a bare glassy carbon electrode (GCE), a GCE modified with CNT, CNT-2/Cu/C, CNT-2/Cu/C/NIP, CNT/MIP, and CNT-2/Cu/C/MIP; (**c**) a GCE modified with CNT-2/Cu/C/MIP and CNT-2/Cu/C/MIP before elution.

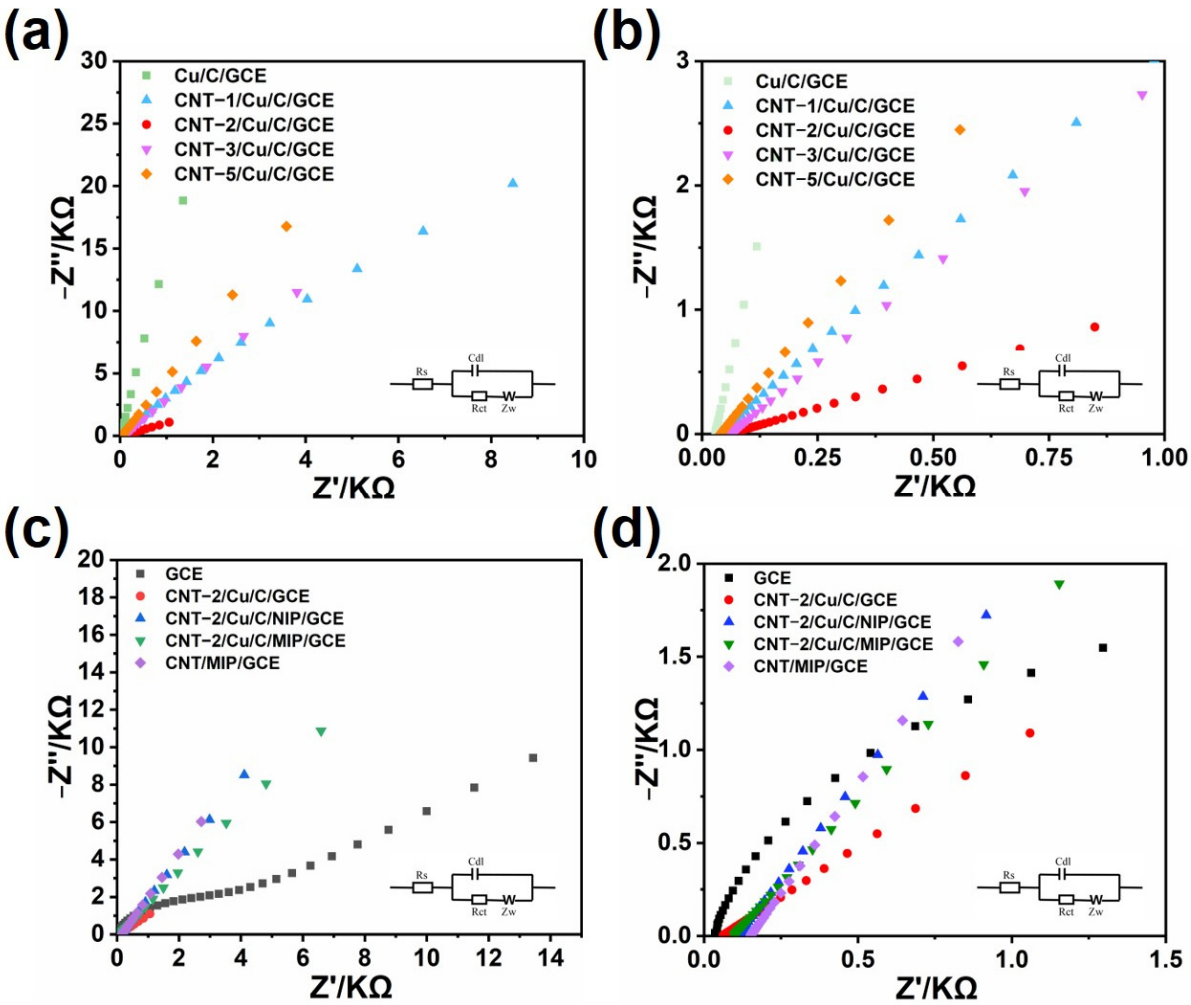

Figure 9. The EIS plots for each electrode modification were obtained in a solution containing 5 mM $[Fe(CN)_6]^{3-/4-}$ and 0.1 M KCl. (**a**) The plots included a bare glassy carbon electrode (GCE), a GCE modified with CNT-2/Cu/C, CNT-2/Cu/C/NIP, CNT/MIP, and CNT-2/Cu/C/MIP, as well as their (**b**) magnified sections. (**c**) A GCE modified with Cu/C, CNT-1/Cu/C, CNT-2/Cu/C, CNT-3/Cu/C, and CNT-5/Cu/C, as well as their (**d**) magnified sections.

Differential pulse voltammetry (DPV) was used to investigate the response of the glassy carbon electrode and modified electrodes to the detection of 4,4′-oxydianiline (Figure 10). The bare GCE electrode (curve a) did not exhibit any reaction to 4,4′-ODA. Modification with calcination resulted in the material of CNT-1/Cu/C with Cu nanocomposite and CNT tubular CNTs, which exhibited a significant improvement in the current response. This modification led to a significant increase in current response (70 µA) compared to the unmodified electrode (trace b). After modification with CNT-2/Cu/C, a significant increase in measurement was observed, as evidenced by the oxidation peak of 95 µA (trace c). This increase was due to the enhanced electron transfer rate and larger specific surface area of the composite electrode. However, with an increase in the amount of CNT, the peak current gradually decreased (trace e). The electrochemical performance of the electrode was further improved by combining CNT-2/Cu/C with MIPs, resulting in a maximum current response of 115 µA (curve g). After removing the template molecule, the MIPs created multiple imprinted cavities that match the structure of 4,4′-ODA and have the ability to selectively detect 4,4′-ODA via hydrogen bonding. The CNT-2/Cu/C/MIP/GCE exhibits superior electrochemical reactivity to 4,4′-ODA compared to CNT-2/Cu/C/NIP/GCE. The polymer membrane surface in CNT-2/Cu/C/NIP/GCE lacks a molecularly imprinted cavity, resulting in the absence of a specific recognition site for detecting 4,4′-ODA.

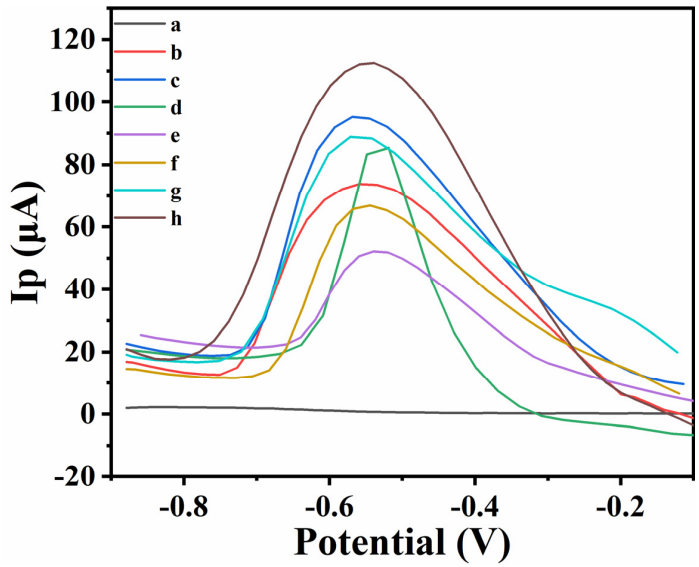

Figure 10. The DPV electrochemical behavior curve of each modified electrode was measured in a 0.1 M PBS solution at pH 7 with a constant concentration of 4,4′-ODA at 10 µM. The electrodes tested included a bare GCE (a), CNT-1/Cu/C/GCE (b), CNT-2/Cu/C/GCE (c), CNT-3/Cu/C/GCE (d), CNT-5/Cu/C/GCE (e), CNT/MIP/GCE (f), CNT-2/Cu/C/NIP/GCE (g), and CNT-2/Cu/C/MIP/GCE (h).

3.3. Analytical Application of CNT-2/Cu/C/MIP/GCE for 4,4′-ODA

The CNT-2/Cu/C/MIP/GCE electrode was modified and used to quantitatively detect 4,4′-ODA under optimized experimental conditions. The oxidation peak current remained discernible even at lower concentrations of 4,4′-ODA. Quantitative analysis was performed using DPV in a pH 7 PBS buffer due to its heightened sensitivity and reduced background current compared to traditional CV techniques. Figure 11a, shows a clear correlation between the amount of 4,4′-ODA and the peak current, ranging from 0.15 µM to 10 µM and from 10 µM to 100 µM. The relationship is expressed by the following equations: Ip(µA) = 10.05C(µM) − 0.27 (R^2 = 0.998) and Ip(µA) = 0.21C(µM) + 98.78 (R^2 = 0.997) (Figure 3b,d). The Limit of Detection (LOD) of 0.05 µM (S/N = 3) was determined using LOD = (3 × standard deviation of peak current in blank PBS solution (n = 10))/slope of the calibration curve of 4,4′-ODA. The sensor fabricated with CNT-2/Cu/C/MIP/GCE

demonstrated a remarkable linear range and a low limit of detection, highlighting its analytical usefulness for accurately quantifying 4,4′-ODA.

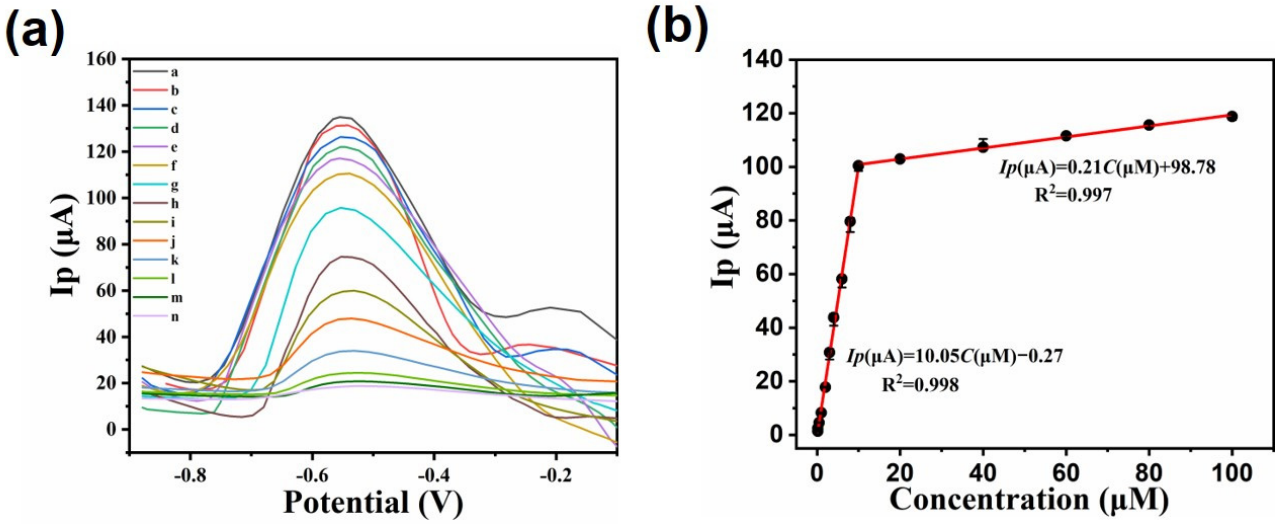

Figure 11. (**a**) DPV curves of CNT-2/Cu/C/MIP/GCE in a 0.1 M PBS buffer with pH of 7 with varying concentrations of 4,4′-ODA under ideal experimental settings. (**b**) Linear relationship between 4,4′-ODA at different concentrations and I_P. The concentrations (a–n) range from 0.15 to 100 μM.

3.4. Selectivity Assessment of the Imprinted Sensor

The specificity of the CNT-2/Cu/C/MIP/GCE electrochemical sensor towards 4,4′-ODA was assessed by comparing molecules of comparable sizes and having the same or similar functional groups that could potentially disrupt the detection of the desired molecule. To assess this, DPV current responses of various potential interferents were compared both individually and in a mixed state in a PBS solution containing 10 μM 4,4′-ODA at a 10-fold concentration (100 μM). The potential interferents assessed for detecting 4,4′-ODA comprised methionine, 4,4′-methylenedianiline, biphenyl, urea, and benzidine. Figure 12 illustrates the current response and peak contrast of these interferents.

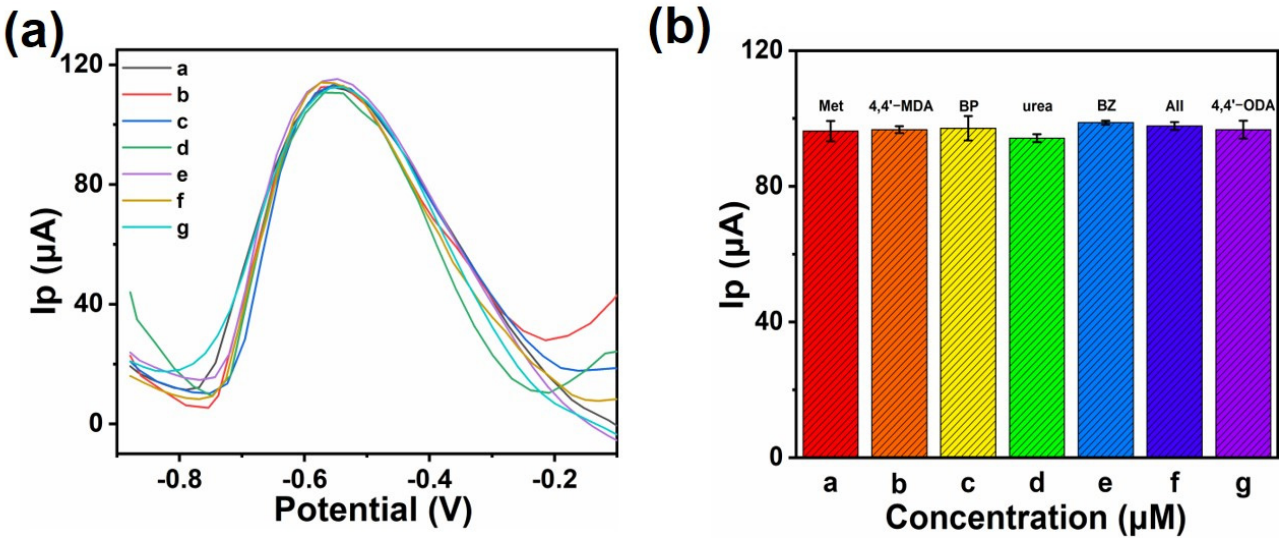

Figure 12. (**a**) The DPV signal of CNT-2/Cu/C/MIP/GCE in response to 10 μM 4,4′-ODA (with background subtracted) and (**b**) the bar graph showing peak current and potential interferents in the buffer solution at 10 times their concentration under ideal experimental conditions. The potential interferents include (a) methionine(Met), (b) 4,4′-methylenedianiline(4,4′-MDA), (c) biphenyl(BP), (d) urea, (e) benzidine(BZ), (f) all, and (g) 4,4′-Oxydianiline(4,4′-ODA).

It was observed that methionine, 4,4′-methylenedianiline, and biphenyl exerted minimal influence on the measurement of 4,4′-ODA. Nonetheless, there was a small amount of interference from urea and benzidine. Urea, benzidine, and 4,4′-ODA share similar molecular structures and functional groups, but urea is smaller in size than 4,4′-ODA. The difference in size could allow urea to reach and attach to the binding site, which could affect the electrochemical measurement of 4,4′-ODA by the imprinting sensor. In order to determine the specificity of the detection system, various potential interferences were introduced at the same time, resulting in reliable quantitative analysis results.

3.5. Sensor Reproducibility and Stability

The sensor made of CNT-2/Cu/C/MIP/GCE showed great consistency in detecting 10 μM 4,4′-ODA in five successive trials, resulting in a relative standard deviation (RSD) of 3.5% for DPV current. Additionally, five different electrodes, prepared under optimized conditions, exhibited satisfactory reproducibility with an RSD of 4.8% for DPV values recorded after the adsorption of 10 μM 4,4′-ODA. Monitoring the DPV response towards 10 μM 4,4′-ODA every 7 days showcased the sensor′s stability. Initially, the modified electrode displayed a consistent electrochemical response, followed by refrigeration at 4 °C. Over subsequent 7-day intervals, the peak current decreased marginally: by 1.2% after 7 days, 3.4% after 14 days, and 5.6% in the fourth period, indicating relatively stable performance. The enduring capability of CNT-2/Cu/C/MIP/GCE highlights its promise for extended monitoring of 4,4′-ODA.

3.6. Real Sample Test

In order to more accurately assess the functionality of the constructed CNT-2/Cu/C/MIP/GCE sensor, the developed sensor was subjected to a spiking recovery test and LC-MS/MS analysis. Given that no 4,4′-ODA was detected in the sample, the standard addition method was employed to assess the potential of the CNT-2/Cu/C/MIP/GCE sensor in real-world applications. The outcomes of the proposed method were validated by comparison with the 4,4′-ODA calibration curve. Table 1 illustrates the exemplary performance of the CNT-2/Cu/C/MIP/GCE, with 4,4′-ODA recovery rates ranging from 86.3% to 103.5%. Similar experiments conducted using LC-MS/MS produced comparable results. In comparison to previous electrochemical methods, including those based on molecularly imprinted sensors (see Table 2) for the determination of 4,4′-ODA as reported in the literature, the sensor demonstrated a high sensitivity and a wide linear range for the detection of 4,4′-ODA. This can be attributed to the integration and synergy effect of these functional materials. These findings underscore the sensor's potential for detecting 4,4′-ODA migration in standard packaging laboratory settings, rendering it suitable for quality control purposes.

Table 1. The recovery of real samples detected by CNT-2/Cu/C/MIP/GCE and LC-MS/MS (n = 3).

Sample	Method	No.	Add (μM)	Found (μM)	Recovery (%)	RSD (%)
Nylon Spatula Sample 1	—		0	—	—	—
	Electrochemical Sensor	1	4	4.14	103.5	1.58
		2	6	6.06	101.0	0.51
		3	10	9.97	99.7	3.99
	LC-MS/MS	1	4	4.05	101.25	1.26
		2	6	6.06	101	0.45
		3	10	9.98	99.8	3.65

Table 1. *Cont.*

Sample	Method	No.	Add (μM)	Found (μM)	Recovery (%)	RSD (%)
Nylon Spatula Sample 2	—		0	—	—	—
	Electrochemical Sensor	1	4	4.06	101.5	3.01
		2	6	5.83	97.2	1.57
		3	10	9.63	96.3	4.25
	LC-MS/MS	1	4	3.96	99.0	2.62
		2	6	5.90	98.3	1.46
		3	10	9.85	98.5	3.85
Nylon Spatula Sample 3	—		0	—	—	—
	Electrochemical Sensor	1	4	3.99	99.8	2.82
		2	6	5.18	86.3	3.01
		3	10	9.81	98.1	2.98
	LC-MS/MS	1	4	4.08	102	2.52
		2	6	5.68	94.7	2.88
		3	10	9.92	99.2	2.43

"—": not found.

Table 2. Comparison of electrochemical analysis methods for determination of 4,4′-ODA.

Electrode	Method	Linear Range (μM)	Detection Limit (μM)	Reference
4,4′–DIADPE–MIP–G–PCEs	Interfacial potentiometry with double poles	0.10–500 μM	0.0463	[41]
C18 modified Au electrode C8 modified Au electrode	SWV	0.05–1.50 0.1–1	0.04 0.06	[42]
MoS_2/GCE	DPV	0.24–1	0.08	[43]
CNT-2/Cu/C/MIP/GCE	DPV	0.15–10, 10–100	0.05	This work

4. Conclusions

This study presents a novel electrochemical sensor tailored for the rapid detection of 4,4′-ODA, a potential carcinogenic primary aromatic amine, offering a wide detection range and a low limit of detection. The sensor's working electrode was augmented by surface modification with pyrolyzed copper/carbon material derived from Cu-BTC MOF and carbon nanotubes (CNTs), resulting in increased surface area and electroconductivity, thereby enhancing electrocatalytic performance. The incorporation of molecularly imprinted polymers (MIPs) further enhances the sensor's selectivity for 4,4′-ODA. The electrochemical sensor CNT-2/Cu/C/MIP/GCE demonstrates a significant linear correlation across a concentration range of from 0.15 μM to 10 μM and from 10 μM to 100 μM under optimal experimental conditions, with a detection limit of 0.05 μM (S/N = 3). The sensor exhibits outstanding sensitivity, detection threshold, and durability for precise measurement of 4,4′-ODA. Real sample experiments validate the reliability of the CNT-2/Cu/C/MIP/GCE in quantifying 4,4′-ODA. Therefore, its robust performance, combined with enhanced specificity and sensitivity, positions it as a crucial tool for advancing safety standards in the plastic manufacturing industry. Future research endeavors could explore real-world applications and broaden the sensor platform to detect other relevant compounds across diverse matrices.

Author Contributions: X.Z.: conceptualization, methodology, formal analysis, investigation, data curation, writing, and original draft preparation; P.Y.: methodology, formal analysis, and investigation; Z.H., C.Y. and J.R.: resources, validation, and supervision; J.W.: conceptualization, funding acquisition, and writing—review and editing; S.T.: data curation and investigation. All authors have read and agreed to the published version of the manuscript.

Funding: This research was funded by the Science and Technology Program Project of the Zhejiang Administration for Market Regulation, grant number ZC2021A015.

Institutional Review Board Statement: Not applicable.

Informed Consent Statement: Not applicable.

Data Availability Statement: The original contributions presented in the study are included in the article material, further inquiries can be directed to the corresponding author.

Acknowledgments: The authors acknowledge the laboratory room support provided by Zhejiang Institute of Product Quality and Safety Science.

Conflicts of Interest: The authors declare no conflicts of interest.

References

1. The European Commission. Commission Regulation (EC) No 552/2009 of 22 June 2009 amending Regulation (EC) No1907/2006 of the European Parliament and of the Council on the Registration, Evaluation, Authorisation and Restriction of Chemicals(REACH) as regards Annex XVII, 552/2009. *Off. J. Eur. Comm.* **2009**. Available online: https://eur-lex.europa.eu/eli/reg/2009/552/oj (accessed on 15 May 2024).
2. Regulation-2016/1416-EN-EUR-Lex (Europa.eu). Available online: https://eur-lex.europa.eu/eli/reg/2016/1416/oj (accessed on 15 May 2024).
3. IARC Monographs Volume 127: Some Aromatic Amines and Related Compounds. Available online: https://www.iarc.who.int/news-events/iarc-monographs-volume-127-some-aromatic-amines-and-related-compounds/ (accessed on 15 May 2024).
4. IARC Monographs on the Identification of Carcinogenic Hazards to Humans. Available online: https://monographs.iarc.who.int/list-of-classifications (accessed on 15 May 2024).
5. Talaska, G. Aromatic amines and human urinary bladder cancer: Exposure sources and epidemiology. *J. Environ. Sci. Health C Environ. Carcinog. Ecotoxicol. Rev.* **2003**, *21*, 29–43. [CrossRef] [PubMed]
6. EPA/Office of Pollution Prevention and Toxics; High Production Volume Information System (HPVIS) on 4,4′-oxybis-Benzenamine (CAS No: 101-80-4). Available online: https://cdxapps.epa.gov/oms-substance-registry-services/substance-list-details/98 (accessed on 9 November 2009).
7. Zhu, J.P.; Aikawa, B. Determination of aniline and related mono-aromatic amines in indoor air in selected Canadian residences by a modified thermal desorption GC/MS method. *Environ. Int.* **2004**, *30*, 135–143. [CrossRef]
8. Chen, X.L.; Li, Z.B.; Zhu, Y.X.; Xu, J.G. Sensitive fluorimetric method for the determination of aniline by using tetra-substituted amino aluminium phthalocyanine. *Anal. Chim. Acta* **2004**, *505*, 283–287. [CrossRef]
9. Yu, X.P.; Tan, L.; Yu, Y.L.; Xia, Y.; Guan, Z.; Gu, J.; Wang, J.; Chen, H.; Jiang, F. Insights into the hydrated electron generation from UV/aniline: Mechanism and quantum efficiency. *Chemosphere* **2022**, *287*, 132292. [CrossRef]
10. Jayapal, M.; Jagadeesan, H.; Krishnasamy, V.; Shanmugam, G.; Muniyappan, V.; Chidambaram, D.; Krishnamurthy, S. Demonstration of a plant-microbe integrated system for treatment of real-time textile industry wastewater. *Environ. Pollut.* **2022**, *302*, 119009. [CrossRef] [PubMed]
11. BelBruno, J.J. Molecularly imprinted polymers. *Chem. Rev.* **2019**, *119*, 94–119. [CrossRef]
12. Chen, L.X.; Wang, X.Y.; Lu, W.H.; Wu, X.Q.; Li, J.H. Molecular imprinting: Perspectives and applications. *Chem. Soc. Rev.* **2016**, *45*, 2137–2211. [CrossRef] [PubMed]
13. Yang, Y.K.; Yan, W.Y.; Guo, C.X.; Zhang, J.H.; Yu, L.G.; Zhang, G.H.; Wang, X.M.; Fang, G.Z.; Sun, D.D. Magnetic molecularly imprinted electrochemical sensors: A review. *Anal. Chim. Acta* **2020**, *1106*, 1–21. [CrossRef]
14. Çorman, M.E.; Ozcelikay, G.; Cetinkaya, A.; Kaya, S.I.; Armutcu, C.; Özgür, E.; Uzun, L.; Ozkan, S.A. Metal-organic frameworks as an alternative smart sensing platform for designing molecularly imprinted electrochemical sensors. *TrAC Trends Anal. Chem.* **2022**, *150*, 116573. [CrossRef]
15. De Middeleer, G.; Dubruel, P.; De Saeger, S. Molecularly imprinted polymers immobilized on 3D printed scaffolds as novel solid phase extraction sorbent for metergoline. *Anal. Chim. Acta* **2017**, *986*, 57–70. [CrossRef] [PubMed]
16. Cui, Y.H.; Ding, L.; Ding, J. Recent advances of magnetic molecularly imprinted materials: From materials design to complex sample pretreatment. *TrAC Trends Anal. Chem.* **2022**, *147*, 116514. [CrossRef]
17. Kaya, S.I.; Cetinkaya, A.; Ozkan, S.A. Molecularly imprinted polymers as highly selective sorbents in sample preparation techniques and their applications in environmental water analysis. *Trends Environ. Anal. Chem.* **2023**, *37*, e00193. [CrossRef]

18. Ahmad, R.; Griffete, N.; Lamouri, A.; Felidj, N.; Chehimi, M.M.; Mangeney, C. Nanocomposites of gold nanoparticles@molecularly imprinted polymers: Chemistry, processing, and applications in sensors. *Chem. Mater.* **2015**, *27*, 5464–5478. [CrossRef]
19. Mustafa, Y.L.; Keirouz, A.; Leese, H.S. Molecularly imprinted polymers in diagnostics: Accessing analytes in biofluids. *J. Mater Chem. B* **2022**, *10*, 7418–7449. [CrossRef]
20. Haupt, K.; Rangel, P.X.M.; Bui, B.T.S. Molecularly imprinted polymers: Antibody mimics for bioimaging and therapy. *Chem. Rev.* **2020**, *120*, 9554–9582. [CrossRef]
21. Rao, H.B.; Liu, X.; Ding, F.; Wan, Y.; Zhao, X.; Liang, R.X.; Zou, P.; Wang, Y.Y.; Wang, X.X.; Zhao, Q.B. Nitrogen-doped carbonnanosheet frameworks decorated with Fe and molecularly imprinted polymer forsimultaneous detection of mebendazole and catechol. *Chem. Eng. J.* **2018**, *338*, 478–487. [CrossRef]
22. Del Blanco, S.G.; Donato, L.; Drioli, E. Development of molecularly imprinted membranes for selective recognition of primary amines in organic medium. *Sep. Purif. Technol.* **2012**, *87*, 40–46. [CrossRef]
23. Chen, N.N.; Chen, L.; Cheng, Y.X.; Zhao, K.; Wu, X.H.; Xian, Y.Z. Molecularly imprinted polymer grafted graphene for simultaneous electrochemical sensing of 4,4-methylene diphenylamine and aniline by differential pulse voltammetry. *Talanta* **2015**, *132*, 155–161. [CrossRef]
24. Shi, T.; Cheng, Z.Y.; Liu, T.; Zhang, Y.L. Application of up-conversion molecularly imprinted nanoprobe for selective recognition and straightforward detection of 4- aminobiphenyl. *Spectrochim. Acta A Mol. Biomol. Spectrosc.* **2022**, *265*, 120405. [CrossRef]
25. Couto, R.A.S.; Costa, S.S.; Mounssef, B.; Pacheco, J.G.; Fernandes, E.; Carvalho, F.; Rodrigues, C.M.P.; Delerue-Matos, C.; Braga, A.A.C.; Gonçalves, L.M.; et al. Electrochemical sensing of ecstasy with electropolymerized molecularly imprinted poly(o-phenylenediamine) polymer on the surface of disposable screen-printed carbon electrodes. *Sens. Actuators B Chem.* **2019**, *290*, 378–386. [CrossRef]
26. Ghaani, M.; Büyüktaş, D.; Carullo, D.; Farris, S. Development of a New Electrochemical Sensor Based on Molecularly Imprinted Biopolymer for Determination of 4,4′ -Methylene Diphenyl Diamine. *Sensors* **2023**, *23*, 46. [CrossRef] [PubMed]
27. Lu, L.J.; Ning, H.Y.; Guo, J.P.; Guo, C.; Pan, L.; Lu, L.X. Synthesis, Evaluation, and Electrochemical Detection Application of Magnetic Molecularly Imprinted Polymers for 4,4′-Methylenedianiline from Food-Contact Materials. *Adv. Polym. Technol.* **2023**, *2023*, 9306542. [CrossRef]
28. Liu, Y.; Dang, X.P.; Ding, H.Y.; Chen, H.X. Specific recognition and solid phase extraction of three primary aromatic amines based on molecularly imprinted polymer monolith for the migration detection in food contact materials. *Microchem. J.* **2022**, *182*, 107895. [CrossRef]
29. Yu, X.L.; Liu, H.; Diao, J.X.; Sun, Y.; Wang, Y.C. Magnetic molecularly imprinted polymer nanoparticles for separating aromatic amines from azo dyes-Synthesis, characterization and application. *Sep. Purif. Technol.* **2018**, *204*, 213–219. [CrossRef]
30. Liu, Y.; Dang, X.P.; Zhang, S.C.; Hu, Y.L.; Chen, H.X. Migration detection of six aromatic amines in polyamide food contact materials by HPLC after molecularly imprinted polymer pipette tip solid phase extraction. *Food. Packag. Shelf.* **2023**, *36*, 101029. [CrossRef]
31. *GB 31604.52-2021*; National Standard for Food Safety—Determination of the Migration of Aromatic Primary Amines from Materials and Products in Contact with Food. National Standard of the People's Republic of China: Beijing, China, 2021.
32. Lei, Y.L.; Shu, Y.J.; Peng, J.H.; Tang, Y.J.; Huo, J.C. Synthesis and properties of low coefficient of thermal expansion copolyimides derived from biphenyltetracarboxylic dianhydride with p-phenylenediamine and 4,4′-oxydialinine. *E-Polymer* **2016**, *16*, 295–302. [CrossRef]
33. Zeinali, S.; Homayoonnia, S.; Homayoonnia, G. Comparative investigation of interdigitated and parallel-plate capacitive gas sensors based on Cu-BTC nanoparticles for selective detection of polar and apolar VOCs indoors. *Sens. Actuat. B Chem.* **2019**, *278*, 153–164. [CrossRef]
34. Deng, T.; Men, X.L.; Jiao, X.C.; Wang, J. CNTs decorated Cu-BTC with catalytic effect for high-stability lithium-sulfur batteries. *Ceram. Int.* **2022**, *48*, 4352–4360. [CrossRef]
35. Shi, Z.D.; Sheng, J.; Yang, Z.Y.; Liu, Z.Y.; Chen, S.; Wang, M.; Wang, L.D.; Fei, W.D. Facile synthesis of high-performance carbon nanosheet/Cu composites from copper formate. *Carbon* **2020**, *165*, 349–357. [CrossRef]
36. Hassan, S.E.D.; Salem, S.S.; Fouda, A.; Awad, M.A.; El-Gamal, M.S.; Abdo, A.M. New approach for antimicrobial activity and bio-control of various pathogens by biosynthesized copper nanoparticles using endophytic actinomycetes. *J. Radiat. Res. Appl. Sci.* **2018**, *11*, 262–270. [CrossRef]
37. Gao, L.L.; Cao, Y.X.; Wang, J.; Ren, H.B.; Wang, J.H.; Huang, J.R. Construction of polypyrrole coated hollow cobalt manganate nanocages as an effective sulfur host for lithiumsulfur batteries. *Ceram. Int.* **2020**, *46*, 18224–18233. [CrossRef]
38. Wang, Y.G.; Lu, Y.; Luo, R.J.; Zhang, Y.G.; Guo, Y.; Yu, Q.H.; Liu, X.M.; Kim, J.K.; Luo, Y.S. Densely-stacked N-doped mesoporous TiO_2/carbon microsphere derived from outdated milk as high performance electrode material for energy storages. *Ceram. Int.* **2018**, *44*, 16265–16272. [CrossRef]
39. Wang, Y.C.; Wei, Y.H.; Wang, B.Y.; Jing, P.; Zhang, Y.; Zhang, Y.; Wang, Q.; Wu, H. Bio-assisted engineering of hierarchical porous carbon nanofiber host in-situ embedded with iron carbide nanocatalysts toward high-performance Li–S batteries. *Carbon* **2021**, *177*, 60–70. [CrossRef]
40. Hu, P.F.; Yuan, A.H.; Meng, C.F.; Chen, H.T.; Zhou, H. Strategies to optimize the lithium storage capability of the metal-organic framework copper-1,3,5-trimesic acid (Cu-BTC). *Chemelectrochem* **2020**, *7*, 4003–4009. [CrossRef]

41. Ma, M.M.; Zhang, Y.; Liu, J. Adsorption of 4,4′-diaminodiphenyl ether on molecularly imprinted polymer and its application in an interfacial potentiometry with double poles sensor. *Chem. Pap.* **2022**, *76*, 1691–1705. [CrossRef]
42. Domínguez, C.S.H.; Vicente, C.Q.J.; Hernández, P.; Hernández, L. Sub-monolayer assemblies of octanethiol and octadecylthiol at gold electrodes for the direct analysis of 4,4′-oxydianiline in wastewaters and shoe-dyeing samples. *Talanta* **2008**, *74*, 1014–1019. [CrossRef]
43. Pozo, M.D.; Sánchez-Sánchez, C.; Vázquez, L.; Blanco, E.; Petit-Domínguez, M.D.; Martín-Gago, J.Á.; Casero, E.; Quintana, C. Differential pulse voltammetric determination of the carcinogenic diamine 4,4′-oxydianiline by electrochemical preconcentration on a MoS_2 based sensor. *Microchim. Acta* **2019**, *186*, 793. [CrossRef]